# Histone H3 tail charge patterns govern nucleosome condensate formation and dynamics

Erin F. Hammonds[1], Anurag Singh[2], Krishna K. Suresh[3], Sean Yang[3], Sarah S. Meidl Zahorodny[1], Ritika Gupta[2], Davit A. Potoyan[3]*, Priya R. Banerjee[2]*, Emma A. Morrison[1]*

[1]Department of Biochemistry, Medical College of Wisconsin, 8701 Watertown Plank Rd., Milwaukee, WI 53226
[2]Department of Physics, The State University of New York at Buffalo, Buffalo, NY 14260
[3]Department of Chemistry, Iowa State University, Ames, IA 50011
*Corresponding: emorrison@mcw.edu, prbanerj@buffalo.edu, potoyan@iastate.edu

## ABSTRACT

Emerging models of nuclear organization suggest that chromatin forms functionally distinct microenvironments through phase separation. As chromatin architecture is organized at the level of the nucleosome and regulated by histone post-translational modifications, we investigated how these known regulatory mechanisms influence nucleosome phase behavior. By systematically altering charge distribution within the H3 tail, we found that specific regions modulate the phase boundary and tune nucleosome condensate viscosity, as revealed by microscopy-based assays, microrheology, and simulations. Nuclear magnetic resonance relaxation experiments showed that H3 tails remain dynamically mobile within condensates, and their mobility correlates with condensate viscosity. These results demonstrate that the number, identity, and spatial arrangement of basic residues in the H3 tail critically regulate nucleosome phase separation. Our findings support a model in which nucleosomes, through their intrinsic properties and modifications, actively shape the local chromatin microenvironment—providing new insight into the histone language in chromatin condensates.

## INTRODUCTION

Dynamic chromatin organization is being re-examined through the lens of phase separation[1–4]. Current models invoke phase separation and biomolecular condensates in subcompartmentalization and the formation of localized environments that are functionally distinct within the nucleus, which dynamically change in response to stimuli[2,3,5–8]. Chromatin regions ranging from transcriptionally-silenced heterochromatin to transcriptionally-active super-enhancers form phase-separated regions[9,10], and condensates with such diverse functions have varied physicochemical properties[11]. It is appealing to consider a model wherein the nucleus exists as a collection of different phase-separated regions, each enriched in a distinct set of chromatin, epigenetic modifications, proteins, and RNA that determine the local environment and the biological activity within it.

The nucleus is rich in multivalent biopolymers capable of undergoing phase separation, and chromatin is no exception with its histone and DNA components. Chromatin can undergo phase separation in the absence of chromatin-interacting proteins, and this holds true even down to the level of the nucleosome core particle (NCP), the basic subunit of chromatin[6,12–17]. Within the NCP, DNA wraps around a folded histone core and the intrinsically disordered termini, or tails, of the histones protrude. The histone tails are enriched in basic residues—the histone tails range from 11-36 residues in length and are 31-42% lysines and arginines while only 0-8% aspartates and glutamates. Chromatin phase separation is driven, at least in part, by interactions between these highly basic histone tails and DNA[6,12,17].

Chromatin organization is regulated by epigenomic modifications, including post-translational modifications (PTMs) on histone proteins[18–20]. Histone PTMs can modulate phase separation within the nucleus[6,21]. Charge-modulating PTMs of histone tail lysines and arginines, including acetylation and other acylation of lysine and citrullination of arginine, alter chromatin compaction and are poised to disrupt the multivalent electrostatic interactions between histone tails and DNA that drive nucleosome phase separation[22,23]. While both carry a single positive charge at neutral pH, lysine and arginine are not identical in terms of interactions with DNA. Arginines are generally thought to form stronger interactions with DNA due to more favorable enthalpic contributions with the phosphate backbone, a greater hydrogen-bonding capacity, a greater propensity for cation-$\pi$ interactions, and a lower energetic cost of desolvation[24–26]. Greater compaction and condensation have been observed with arginine-rich than lysine-rich peptides[27–32]. The more favorable interaction of arginines with DNA holds true in simulations of NCPs and nucleosomes[33–35]. What is the relative role of histone tail lysines and arginines in nucleosome condensate formation and dynamics?

Here, we begin to systematically dissect the influence of lysines and arginines and their charge-neutralizing modifications by investigating the role of basic residues of the H3 tail, the longest of the core histone tails[36], on nucleosome phase separation. In the case of the H3 tail, six lysines and four arginines are distributed along its length with the potential to contribute to phase separation via interactions with DNA. We divide the H3 tail into three regions to investigate the position-dependent effect of perturbing lysines or arginines in the most N-terminal region (residues preceding the first TGG repeat) or central region (residues between the two TGG repeats) on nucleosome phase separation. Basic residues are perturbed in these regions via neutralizing mutations to glutamine as mimetics for acetylation and citrullination or by converting all basic residues to one type (i.e. either all lysines or all arginines). Using microscopy-based techniques in conjunction with simulations, we demonstrate that the number and position of lysine and arginine neutralizations within the H3 tail determines nucleosome phase boundaries and the viscosity of their condensates. NMR dynamics experiments show minimal differences in picosecond-to-nanosecond timescale dynamics of the H3 tail within condensates and display a correlation between condensate viscosity and H3 tail dynamics. Together, these data support a model wherein nucleosomes are actively involved in defining the local chromatin microenvironment, which can be tuned via charge-modulating histone PTMs.

## RESULTS

### Nucleosome core particle phase boundary shifts with basic residue neutralization in a position-dependent manner.

We started by investigating the role of charge neutralization of H3 tail arginines and lysines and the distribution of these neutralizations along the tail on NCP phase separation (**Figure 1**). Mutations to glutamine were used, which serve as mimetics for the PTMs arginine citrullination and lysine acetylation. We designed mutants (**Figure 1A**) to test a model wherein the most N-terminal basic residues in the tail have more potential to form inter-nucleosomal interactions and facilitate phase separation than the basic residues in the center of the tail sequence. We used the TGG repeats to define boundaries between what we will refer to here as the 'terminal', 'central', and 'hinge' regions, and designed mutants to separately neutralize arginines and lysines within the terminal region (R2/8Q-H3 and K4/9Q-H3) and central region (R17/26Q-H3 and K14/18/23/27Q-H3) (**Figure 1A**). Additionally, we designed mutants with neutralization of all four arginine residues (R2/8/17/26Q-H3), the four lysine residues adjacent to arginine residues (K4/9/18/27Q-H3), and all six lysine residues (K4/9/14/18/23/27Q-H3) across the terminal and central regions.

To probe the effect of charge-neutralizing mutations of H3 tail basic residues on NCP phase separation, turbidity and brightfield microscopy were used along with concentration measurements from centrifugation-based assays to monitor droplet formation and determine the phase boundary of each mutant-H3-NCP. These assays were conducted at 25-28°C and at physiologically-relevant salt concentrations of 150 mM KCl and 2 mM $MgCl_2$, and the turbidity and microscopy were collected for a range of discrete NCP concentrations from 0 to 300 μM. As the point of comparison for all mutants, droplets were observed via brightfield microscopy at unmodified-NCP concentrations of 50 μM and greater, which is also in agreement with sample turbidity (**Figure 1C-D, Supplementary Figure 1**). Note that this boundary is shifted to lower concentrations from our previous publication due to the inclusion of $MgCl_2$ [12]. The phase boundary for unmodified-NCP was measured with a light phase concentration ($c_L$) of 60 ± 20 μM and dense phase concentration ($c_D$) of 1000 ± 100 μM (**Figure 1E, Supplementary Figure 1, Supplementary Table 1**). Previously, we reported that joint removal of the terminal and central regions of the H3 tail abrogated phase separation in the presence of 150 mM KCl[12]. Here, we confirmed that phase separation was similarly abrogated for tailless-H3-NCP concentrations up to 300 μM in the presence of 2 mM $MgCl_2$ by the lack of turbidity and droplets along with the presence of only a single-phase measuring at the input concentration following centrifugation (**Figures 1C-E, Supplementary Table 1**). We interpret these results to support the importance of the H3 tail in NCP phase separation under the experimental conditions tested.

H3 tail arginine neutralization influences NCP phase separation in a position-dependent manner. Neutralizing the central region arginine residues (R17/26Q-H3-NCP) does not shift the phase separation boundary as compared to unmodified-NCP while neutralizing the terminal region arginine residues (R2/8Q-H3-NCP) shifts the appearance of droplets and turbidity to higher concentrations (100 μM NCP) (**Figure 1C-D, Supplementary Figure 1**). Neutralization of all four arginine residues of the H3 tail (R2/8/17/26Q-H3-NCP) shifts the appearance of droplets and turbidity to at least 100 μM NCP (**Figure 1C-D, Supplementary Figure 1**). The phase boundaries for R2/8Q-H3-NCP were measured at $c_L$ = 100 ± 30 μM and $c_D$ = 960 ± 60 μM and for R17/26Q-H3-NCP at $c_L$ = 70 ± 20 μM and $c_D$ = 980 ± 80 μM, supporting a shift in the onset of phase separation for neutralization of the terminal but not central region arginines (**Figure 1E, Supplementary Table 1)**. Phase boundary measurements support a narrowing of the boundary for R2/8/17/26Q-H3-NCP as compared to unmodified-NCP, with the light phase concentration shifted to higher concentrations ($c_L$ = 90 ± 20 μM) and the dense phase concentration shifted to lower concentrations ($c_D$ = 750 ± 100 μM) (**Figure 1E, Supplementary Table 1)**. By this

approach, the additional neutralization of the two central arginines led to a lowering of the upper concentration boundary.

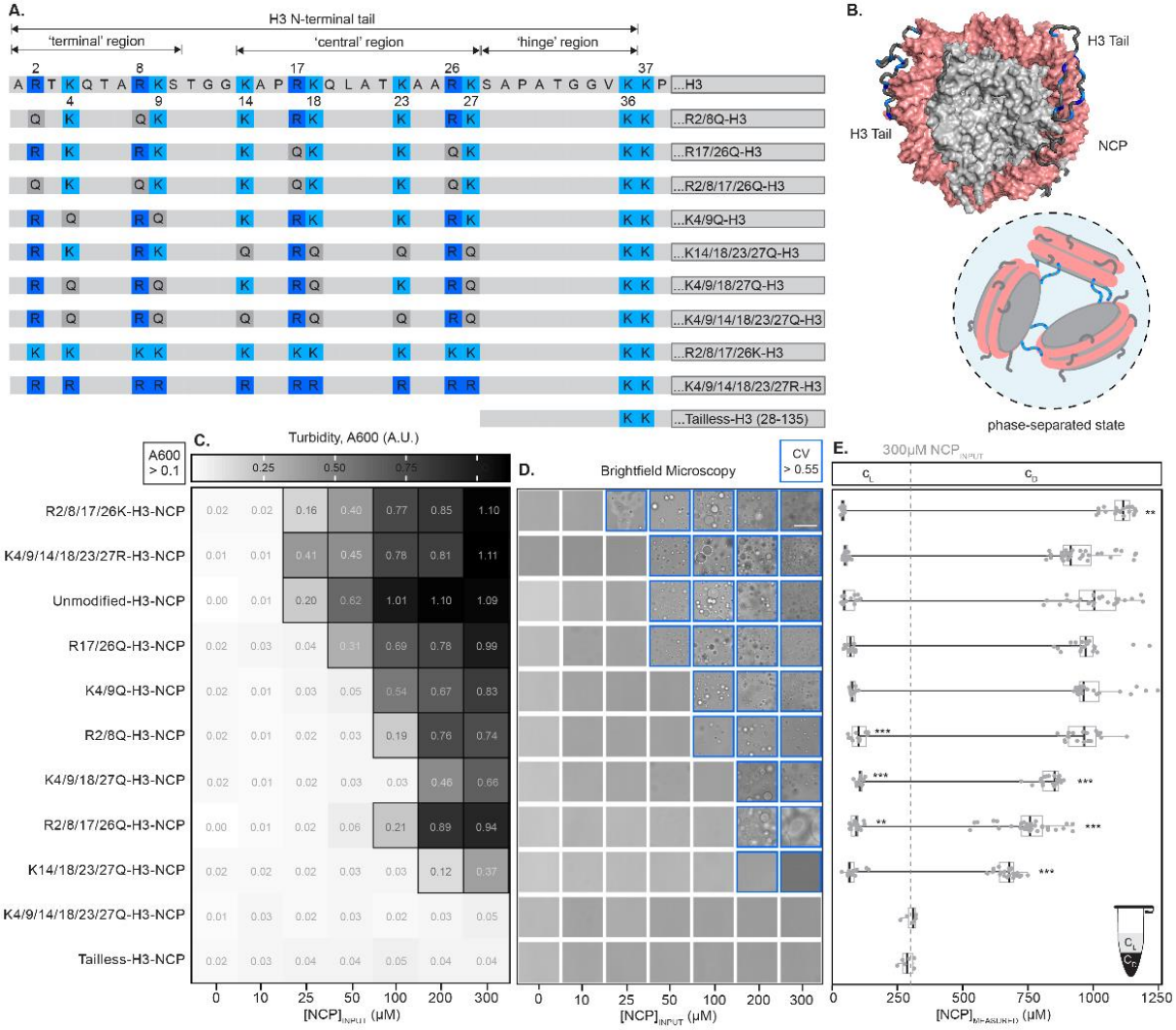


**Figure 1. Nucleosome phase boundary shifts with perturbation of basic residues. A.** Histone H3 tail amino acid sequence that protrudes from the nucleosome core. Arginine (dark blue) and lysine (light blue) residues are highlighted and carried through to mutants below the unmodified-H3 sequence. **B.** NCP with basic residues of H3 tail colored according to (**A**). NCP conformation is from a molecular dynamics simulation end state[37]. **C.** Turbidity (absorbance at 600 nm) values (average of n=3) are shown in greyscale for NCP with unmodified or mutant H3, as labeled, and as a function of NCP concentration. Turbidity is plotted as a heatmap ranging from 0.01 (white) to 1.4 (black). Values greater than 0.1 are outlined with a black square to indicate light scattering due to droplet formation. **D.** Brightfield microscopy images were collected for the same NCP concentrations as in (**C**). The scale bar is 50 µm. A coefficient of variation value (see Methods) was determined for each image. Values greater than 0.55 are considered significant and are outlined in blue to indicate droplets. Full field-of-view images are shown in **Supplementary Figure 1**. **E.** Phase boundary measurements for unmodified and mutant H3-NCPs following induction of phase separation at an input NCP concentration of 300 µM. The concentration of the light phase ($c_L$) and dense phase ($c_D$) were measured following centrifugation at 25°C. In the box plot, the black center vertical line marks the median, the grey box marks the interquartile range (IQR) from the 25$^{th}$ to 75$^{th}$ percentile, and the

grey horizontal lines mark the minimum (25th percentile – 1.5*IQR) and maximum (75th percentile +1.5*IQR). A black line connects the $c_L$ and $c_D$ median values as a visual aid for the phase boundaries. Significance of $c_L$ and $c_D$ for each mutant as compared to unmodified NCP was determined via ANOVA with Tukey post-hoc analysis where *** $p < 0.001$, ** $p < 0.01$, * $p < 0.05$. Those not marked are considered not significant.

Lysine neutralization also influences NCP phase separation in a position-dependent manner. Similar to the terminal arginines, neutralizing the terminal region lysines (K4/9Q-H3-NCP) shifts the appearance of droplets and turbidity to higher concentrations of NCP (100 μM) (**Figure 1C-D, Supplementary Figure 1**). Neutralization of the four central region lysine residues (K14/18/23/27Q-H3-NCP) also shifts the onset of condensates and turbidity to higher concentrations of NCP (200 μM), which is in contrast to the neutralization of the central arginines. This difference may be attributable to a difference in the number of arginines (i.e. two) and lysines (i.e. four) in the central region. Of note, clear droplet morphologies are not observed with this sample. Rather, we observe small clusters at 200 and 300 μM NCP with minimal turbidity. Neutralization of the four arginine-adjacent lysines (K4/9/18/27Q-H3-NCP), which are distributed across both the terminal and central regions, shifts the onset of droplets and turbidity to higher concentrations of NCP and is qualitatively similar to the neutralization of the four arginines. When all six H3 tail lysine residues across the tail are neutralized (K4/9/14/18/23/27Q-H3-NCP), we do not observe phase separation at concentrations up to 300 μM NCP, the highest concentration tested. The phase boundaries for K4/9Q-H3-NCP were measured at $c_L$ = 80 ± 10 μM and $c_D$ = 1000 ± 100 μM, which are not significantly different from unmodified-NCP. Despite not showing clear droplet morphologies, K14/18/23/27Q-H3-NCP did separate into two layers upon centrifugation, allowing measurement of the two phases. While this mutant did not have a significantly shifted light phase concentration ($c_L$ = 80 ± 30 μM) as compared to unmodified-NCP, the dense phase was shifted to lower concentrations ($c_D$ = 670 ± 40 μM) (**Figure 1E, Supplementary Table 1)**. Neutralization of the four arginine-adjacent lysine residues (K4/9/18/27Q-H3-NCP) resulted in a narrowing in the phase boundary, where light phase concentration shifted to higher concentrations ($c_L$ = 110 ± 10 μM) and the dense phase concentration shifted to lower concentrations ($c_D$ = 840 ± 40 μM) compared to unmodified-NCP (**Figure 1E, Supplementary Table 1)**. While this shifted boundary is qualitatively similar to the neutralization of the four arginines, neutralization of the four arginines has a larger effect on $c_D$ (**Supplementary Table 2**), supporting a stronger effect of arginine neutralizations.

Together, these data suggest that the type (i.e. arginine vs. lysine), number (i.e. two vs. four vs. six), and distribution of basic residues (i.e. terminal vs. central vs. both) neutralized each play a role in nucleosome phase separation propensity. Systematic differences were observed throughout between the onset of droplets and turbidity as assessed visually and the $c_L$ measured after centrifugation of phase-separated samples. We speculate that these systematic differences could be due to small differences in temperature and/or an effect of centrifugal forces.

**Arginine and lysine contribution within the H3 tail to nucleosome phase separation.**

To further test the role of H3 tail arginine and lysine residues in nucleosome phase separation, we designed two mutants to convert all basic residues across the terminal and central regions of the H3 tail to only one type: R2/8/17/26K-H3 (all-lysine) and K4/9/14/18/23/27R-H3 (all-arginine) (**Figure 1A**). The same series of experiments as before was carried out on NCPs containing these H3 mutants (**Figure 1C-D, Supplementary Figure 1**). Solution turbidity was measured at NCP concentrations down to 25 μM for both R2/8/17/26K- and K4/9/14/18/23/27R-H3-NCP, and droplets were observed at 25 μM for R2/8/17/26K-H3-NCP. Notably, these are the only mutants tested that shifted the onset of phase separation to lower NCP concentrations than observed for unmodified-NCP. The phase boundaries for R2/8/17/26K-H3-NCP were measured at $c_L$ = 42 ± 7 μM and $c_D$ = 1100 ± 50 μM and for K4/9/14/18/23/27R-H3-NCP at $c_L$ = 50 ± 10 μM and $c_D$ = 950 ± 100 μM (**Figure 1E, Supplementary Table 1**). Across these concentration

measurements, only the $c_D$ for R2/8/17/26K-H3-NCP was significantly different (**Figure 1E**). This all-lysine mutant is the only one tested with an elevated $c_D$ as compared to unmodified-NCP. These data are in agreement with a model wherein arginine and lysine residues within the H3 tail do not contribute equally to NCP phase separation propensity. A mixture of arginine and lysine residues may be important for reasons other than their different modifications and recognition by reader proteins.

**Sequence modifications to the H3 tail influence tail-DNA condensate formation.**

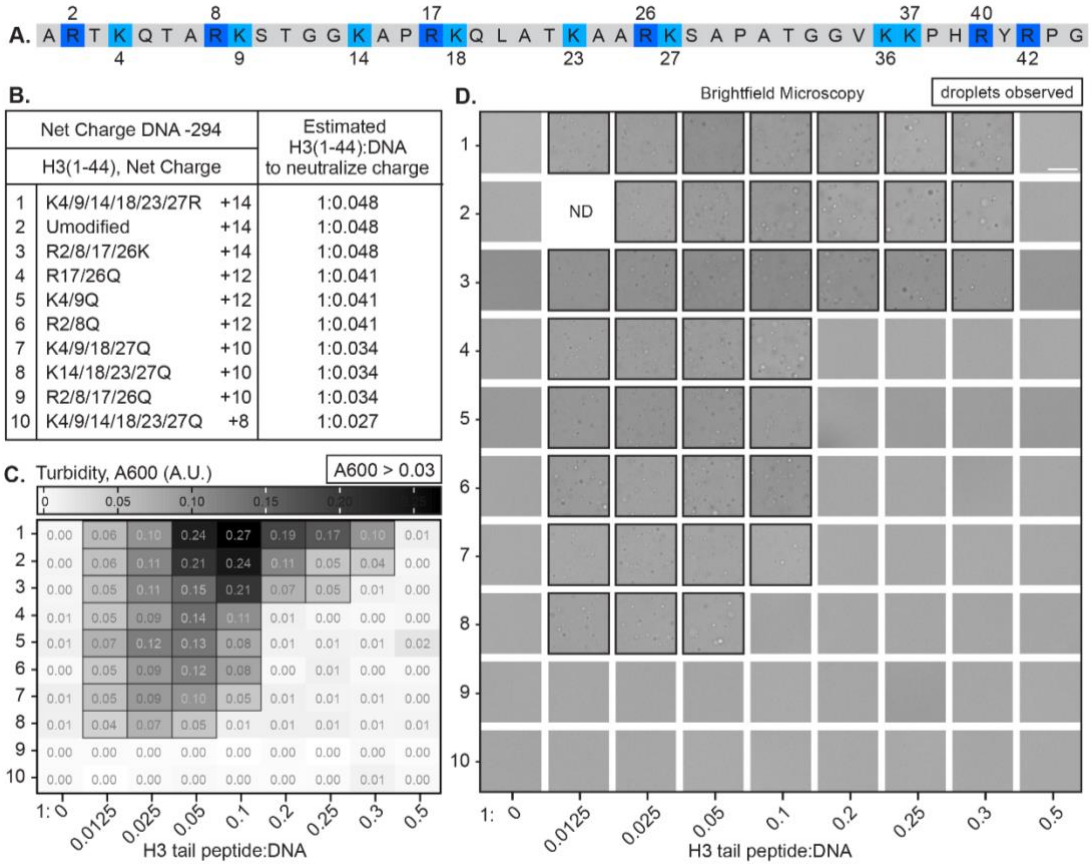


**Figure 2. Phase separation of H3 tail peptide with DNA is also modulated by perturbation of basic residues. A.** Sequence of H3 peptide, H3(1-44), which includes the H3 tail. Basic residues are highlighted as in **Figure 1A**. **B.** Mutants of H3(1-44) are summarized. The same H3 mutations from **Figure 1** were made to H3(1-44). The approximated net charge is listed for 147-bp Widom 601 DNA along with peptides. The molar ratio of peptide:DNA with neutral charge is estimated for each mutant. **C.** Turbidity (absorbance at 600 nm) values (average of n=3) are shown in greyscale for unmodified and mutant versions of H3(1-44) at 50 µM and increasing amounts of 147-bp Widom 601 DNA, shown as molar ratio. **D.** Brightfield microscopy images were collected at the same molar ratios as (**C**). ND = no data. The scale bar is 25 µm. See **Supplementary Figure 2** for an alternative representation of turbidity data and for full field-of-view images. Construct numbering in (**C**) and (**D**) aligns with the table in (**B**).

To further probe the effect of H3 tail modifications, we simplified to a two-component system containing purified H3 tail peptide [residues 1-44, H3(1-44)] and the 147-bp Widom 601 DNA sequence and tested the same mutations as within the context of the nucleosome (**Figure 2A-B**). Previously, we demonstrated that the phase separation behavior of H3 tail peptide with

DNA is similar to the reentrant condensation observed for other systems with multivalent interactions between nucleic acids and arginine- and lysine-rich intrinsically disordered peptides[12,29,30,38–40]. Using turbidity assays and DIC microscopy, we determined the phase boundary for this two-component system and compared it to the estimated charge neutralization ratio for H3(1-44) mutants and 147-bp Widom DNA, which is predicted to display the maximum phase separation if the system follows complex coacervation (**Figure 2B**). Overall, increasing the number of neutralizations shifted and narrowed the phase transition (**Figure 2C-D, Supplementary Figure 2)**. Phase separation near the estimated charge neutralization ratio is seen for all H3 tail peptides except with R2/8/17/26Q and K4/9/14/18/23/27Q mutations, where no phase separation is observed. The loss of phase separation for R2/8/17/26Q-H3(1-44) neutralizations differs from K14/18/23/27Q-H3(1-44) and K4/9/18/27Q-H3(1-44), which have the same total charge, supporting a differential effect between modifications to arginine and lysine. The similarity of R2/8Q and R17/26Q modifications within this simplified two-component system is distinct from the nucleosomal context where R2/8Q had a stronger effect than R17/26Q (**Figure 1C-D**, **Figure 2C-D**). Unmodified-, R2/8/17/26K-, and K4/9/14/18/23/27R-H3(1-44) have the same net charge and displayed a similar position of maximum phase separation, but K4/9/14/18/23/27R-H3(1-44) was distinct in showing a broader transition via turbidity (**Figure 2C**, **Supplementary Figure 2**). These assays emphasize the difference between arginines and lysines in driving condensate formation via H3 tail-DNA interactions and support that the position of neutralizations within the tail is more important within the nucleosomal context.

**Basic residues within the histone H3 tail govern the nucleosome condensate microenvironment.**

We sought to understand how the neutralization of basic residues within the H3 tail influences the microenvironment of nucleosome condensates. Using temperature-controlled video particle tracking (VPT) experiments (**Figure 3A**), we determined the viscosity of NCP condensates. Overall, neutralization of basic residues decreases the viscosity of NCP condensates, and the degree of neutralization correlates with enhanced condensate fluidity (**Figure 3B-C**, **Supplementary Table 3**). We observe a decrease in viscosity when we increase the number of lysine neutralizations (compare unmodified at 110 $\pm$ 10 mPa s to K4/9Q- and K4/9/18/27Q-H3-NCP at 30 $\pm$ 10 and 13 $\pm$ 1 mPa s, respectively) and arginine neutralizations (compare unmodified to R2/8Q-, R17/26Q-, and R2/8/17/26Q-H3-NCP at 27 $\pm$ 2 mPa s, 46 $\pm$ 5 mPa s, and 2.2 $\pm$ 0.6 mPa s, respectively). Neutralization of all four arginine residues within the H3 tail (R2/8/17/26Q-H3-NCP) leads to the lowest measured viscosity among the samples tested. Similar to with the phase boundary measurements, there appears to be a dependence on position. Two arginine residues neutralized in the most ‘terminal’ region (i.e. R2/8Q-H3-NCP) leads to a larger decrease in viscosity than two arginines in the ‘central’ region (i.e. R17/26Q-H3-NCP). Furthermore, we observe the type of residue neutralized influences NCP condensate viscosity in some samples (see R2/8/17/26Q- and K4/9/18/27Q-H3-NCP). Interestingly, NCP with only lysines in the H3 tail (R2/8/17/26K-H3-NCP) has decreased condensate viscosity (83 $\pm$ 5 mPa s) as compared to unmodified-NCP while NCP with only arginines in the H3 tail (K4/9/14/18/23/27R-H3-NCP) is the one modification tested that increases the condensate viscosity (260 $\pm$ 20 mPa s). Notably, there is a global linear correlation between viscosity and $c_L$ with two exceptions: R2/8/17/26K- and R2/8/17/26Q-H3-NCP (**Figure 3D**). These differences may stem from a complex interplay between hydrodynamic effects and sequence-encoded thermodynamic interactions in these systems[41].

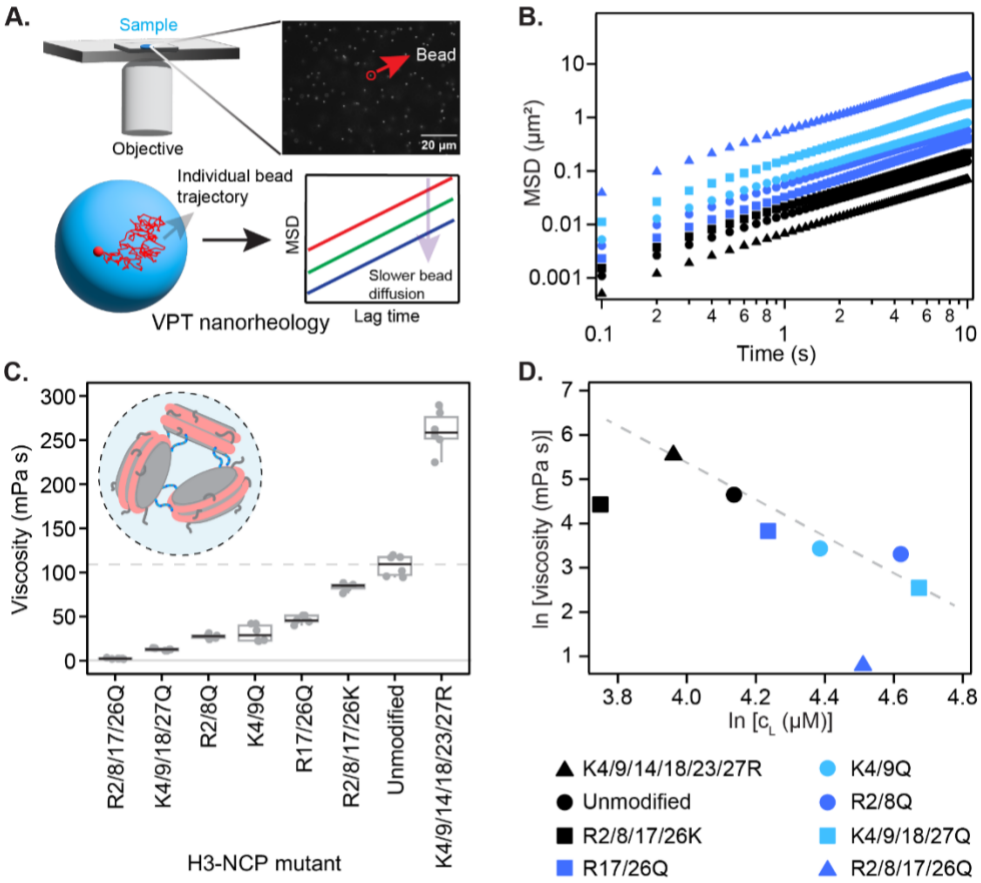


**Figure 3. Condensate viscosity is tuned by H3 tail charge patterns. A.** Schematic representation of the video particle tracking (VPT) microrheology employed to determine the viscosity of condensates formed by unmodified-NCP and H3-NCP mutants. The motion of yellow-green fluorescent carboxylate-modified beads embedded inside condensates were tracked. Individual trajectories of the tracked beads were analyzed to estimate the mean squared displacement (MSD) of the beads. **B.** MSD profiles of the tracked beads in various condensates at 24°C. Shift towards lower MSDs depicts slower diffusivity of the beads inside the dense phases of the NCP variants. **C.** Viscosities of the condensates formed by unmodified-NCP and H3-NCP mutants were estimated from the fit of the MSDs to the equation $MSD = 4D\tau^{\alpha}$. In the box plot, the black center horizontal line marks the median, the grey box marks the interquartile range (IQR) from the 25$^{th}$ to 75$^{th}$ percentile, and the grey vertical lines mark the minimum (25$^{th}$ percentile – 1.5*IQR) and maximum (75$^{th}$ percentile +1.5*IQR). All viscosities are significantly different from unmodified NCP condensates as determined via ANOVA with Tukey post-hoc analysis. Significance is reported in **Supplementary Table 4**. **D.** Inverse correlation between the estimated viscosity and $c_L$ of unmodified and H3-NCP mutants. The dashed grey line is a guide to the eye for the inverse correlation. The figure contains data from measurements at 5-6 randomly chosen positions of the dense phases over two independently prepared sample repeats. Symbols for (**B**) and (**D**) are identified in the lower right.

## Phase behavior and viscosity of H3 tail-DNA condensates from coarse-grained simulations.

The thermodynamic and material properties of H3 tail-DNA condensates were investigated using coarse-grained simulations (**Figure 4A-B**), where each amino acid of the histone tail H3(1-44) and each nucleotide of the double-stranded DNA were coarse-grained into single beads. The phase diagram (**Figure 4C**) shows strong agreement with the experimental results obtained with NCPs (**Figure 1**). The H3 tail mutants with only lysine (R2/8/17/26K) and only arginine (K4/9/14/18/23/27R) display higher critical temperatures compared to the unmodified and all other mutants. With increasing arginine replacement to glutamine (compare

unmodified to R2/8Q and R2/8/17/26Q) both the critical temperature and concentration decrease. The higher critical temperature of the mutant with two arginine residues neutralized in the 'central' region (R17/26Q), compared to the mutant with two arginine residues neutralized in the 'terminal' region (R2/8Q), suggests a positional effect, where the location of arginine-to-glutamine substitutions within the histone tail influences phase separation behavior and condensate stability. Comparing the substitution of all arginine with lysine (R2/8/17/26K) or with glutamine (R2/8/17/26Q), a significant increase in the critical temperature is observed for R2/8/17/26K, along with a broader phase separation boundary (which means the condensate concentration is higher at 300K). The R2/8/17/26Q mutant and its lysine corollary, K4/9/18/27Q, exhibit very similar values of critical temperatures as indicated by the fitting results. The R2/8/17/26Q mutant exhibits the narrowest phase separation boundary compared to all other mutants and the unmodified peptide, which is consistent with the experimental results. The K4/9/14/18/23/27Q mutant is identified by the coarse-grained model as having the lowest critical temperature, while in our experiments, this mutant failed to form condensates (**Figure 1**).

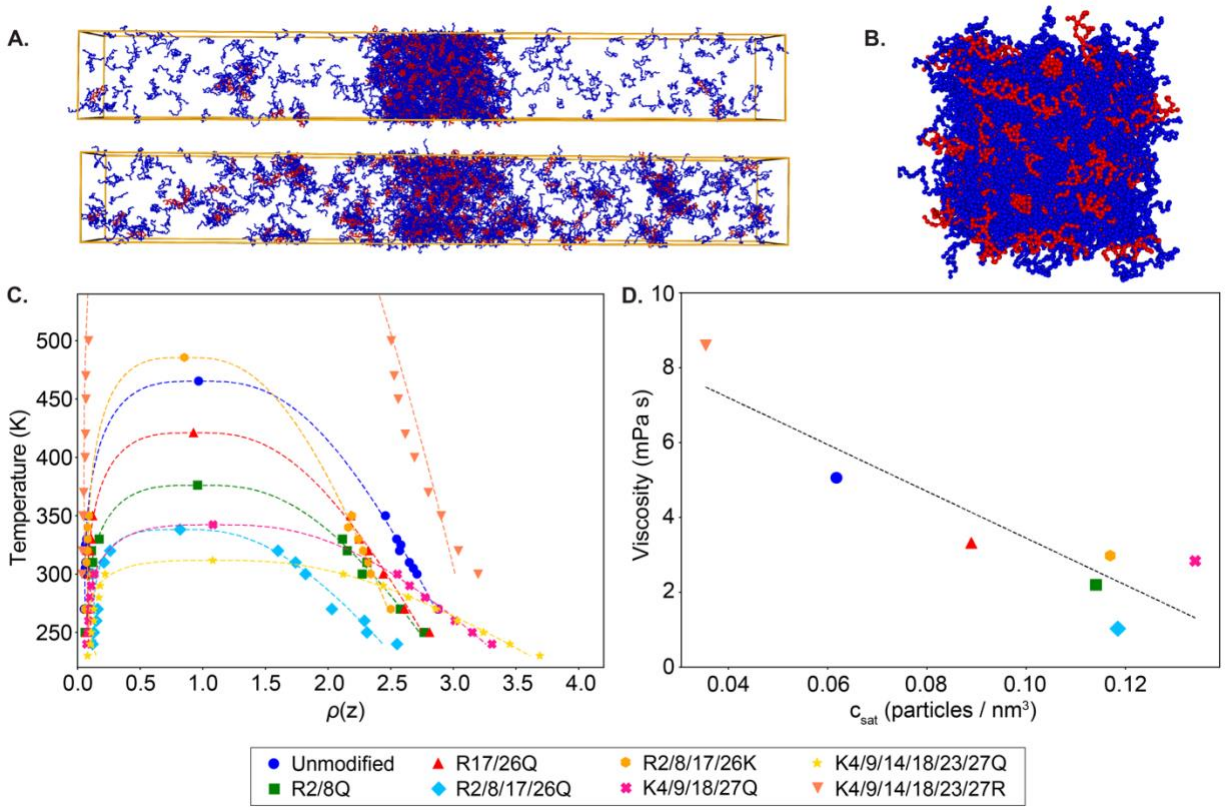


**Figure 4: Phase behavior and viscosity of H3 tail-DNA condensates of unmodified and mutants from coarse-grained MD simulations. A.** Snapshots of R2/8/17/26Q-H3(1-44) (blue) with DNA (red) condensates at 250 K (upper) and 300 K (lower) from coarse-grained simulations, highlighting the transition between condensed and dilute phases. **B.** Snapshot from viscosity calculation simulations performed at 300 K, where the simulation box is systematically shrunk to achieve the condensed-phase density. **C.** Phase diagrams of unmodified-H3 tail peptide and selected mutants with DNA, showcasing the critical temperature and concentrations associated with phase transitions. **D.** Viscosity as a function of saturated concentrations derived from the phase diagram analysis of the unmodified-H3 tail peptide and mutants.

Next, we calculated viscosities from the coarse-grained simulations. The mutant with two arginine residues neutralized in the 'terminal' region (R2/8Q) exhibits lower viscosity compared to the mutant with two arginine residues neutralized in the 'central' region (R17/26Q). The all arginine-to-lysine mutant (R2/8/17/26K) exhibits decreased viscosity compared to the unmodified

H3 tail. The experimental data indicate that the $c_L$ values of R2/8Q and R2/8/17/26Q are relatively close and R2/8/17/26Q has lower viscosity than R2/8Q, an observation that agrees with our simulations as well. We also notice that both R2/8/17/26Q and its lysine counterpart, K4/9/18/27Q, exhibit lower viscosity compared to the unmodified. Among all the mutants tested, the all arginine-to-glutamine mutant (R2/8/17/26Q) exhibited the lowest measured viscosity. The mutant with all lysine-to-arginine (K4/9/14/18/23/27R) has the highest viscosity when compared with all the mutants tested and the unmodified. These results align remarkably well with the experimental observations and support that viscosity exhibits an inverse relationship with saturation concentration ($c_{sat}$) across all studied constructs (**Figure 4D)**.

**H3 tails remain highly mobile in NCP condensates.**

The measured viscosities of the NCP condensates (**Figure 3C**, **Supplementary Table 3**) are at the low end of the values previously reported for biomolecular condensates[42]. While the condensate environment restricts local motions in some systems[43–45], several condensate systems have been reported to display high mobility of intrinsically disordered regions at the molecular level[46,47]. As histone tail dynamics are proposed to be important in the histone language[48,49], we next asked how these functional protein motions are perturbed by the condensate environment. We used solution NMR spectroscopy to investigate the mobility of the H3 tails within NCP condensates. Notably, backbone resonances were still observable for the nucleosomal H3 tails within the dense phase of a phase-separated sample, supporting that the tails retain a high level of mobility within condensates (**Supplementary Figure 3A-B**). However, within the dense phase, resonances for residues towards the ends of the tail broaden largely beyond detection—T3, K4, and V35 are no longer visible. Chemical shift perturbations ($\Delta\delta$) determined from $^{1}$H-$^{15}$N HSQC spectra were minimal between the dense and dilute phases (**Supplementary Figure 3C**). This is commonly observed for IDPs within condensates (e.g. see [43,44,46]). The visibility of resonances in dense phase spectra, along with the minimal changes in chemical environment, support a model wherein the H3 tails remain disordered and bound to DNA in a dynamic ensemble of conformations.

We used NMR spin relaxation experiments to provide insight into nucleosomal H3 tail dynamics on the ps-ns timescale (**Figure 5A-C**). On average, across the tail, $^{15}$N-R1 values increased by 3% and hnNOE values decreased by 12% while $^{15}$N-R2 values increased by 71% in the dense phase as compared to the light phase (**Supplementary Figure 4**). The similarities of the R1 and hnNOE values between the two phases are remarkable. While the signal quality (sensitivity) of hnNOE spectra collected on $^{15}$N-unmodified-H3-NCP samples is especially poor, the hnNOE profiles for the two phases are the same within the error of the experiment (**Figure 5C**, **Supplementary Figure 5**). Thus, while there are only minor, if any, differences between the two phases for $^{15}$N-R1 and hnNOE, the $^{15}$N-R2 values have a strong dependence on phase (**Figure 5A-B**, **Supplementary Figure 5**). The data support that the H3 tails remain highly mobile on the ps-ns timescale within nucleosome condensates while the increased R2 values could reflect the increase in viscosity as well as an increase in inter-nucleosomal as compared to intra-nucleosomal tail-DNA interactions within the dense phase. The R2 profile for residues 26-29 stands out as distinct between the two phases. The difference in R2 profile shape for R26, K27, S28, and A29 suggests the possibility of interesting conformational dynamics changes at the boundary between the ‘central’ and ‘hinge’ regions between the two phases, which could originate from differences between intra- and inter-nucleosomal interactions.

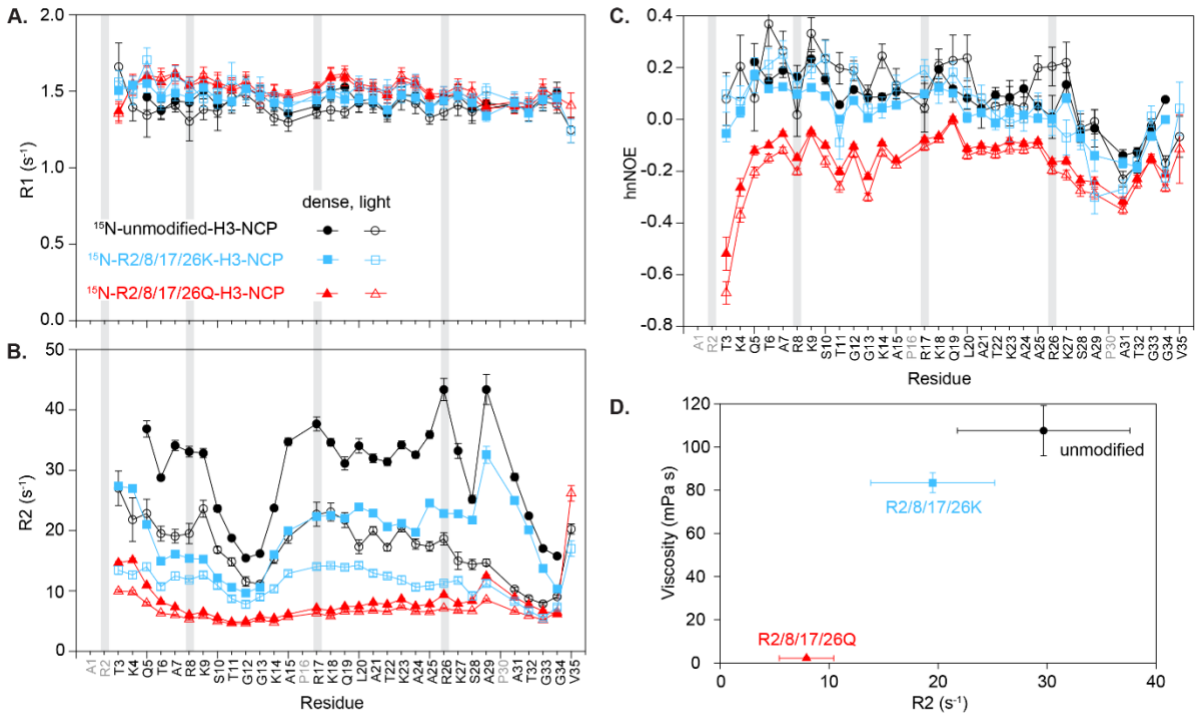


**Figure 5. NMR fast-timescale dynamics indicate highly mobile H3 tails within nucleosome condensates.** Plots are shown for $^{15}$N-R1 rates (**A**),$^{15}$N-R2 rates (**B**), and hnNOE values (**C**) as a function of residue for unmodified- (black circles), R2/8/17/26K- (blue squares), and R2/8/17/26Q- (red triangles) H3-NCP. Data were collected on the light phase (open symbols) and dense phase (closed symbols) of NCP samples prepared in 20 mM MOPS pH 7, 150 mM KCl, 2 mM $MgCl_2$, 0.1 mM EDTA, and 10% $D_2O$. Error bars were determined via the covariance matrix in fitting R1 and R2 decay curves and represent standard error propagation of the spectral noise for hnNOE values. Residues without data for any sample are colored grey in the x-axis labels. Data were collected at 600 MHz and 298 K. **D.** Correlation between viscosity measured via microrheology and average $^{15}$N-R2 rates.

We next investigated the H3 tail dynamics within two of the mutants toward the extremes of condensate changes in our system–either neutralizing the four arginines ($^{15}$N-R2/8/17/26Q-H3-NCP) or switching them to lysines ($^{15}$N-R2/8/17/26K-H3-NCP). Within the light phase, the average $^{15}$N-R1 value increased by 9% or 7%, $^{15}$N-R2 values decreased by 59% or 35%, and hnNOE values decreased by 310% or 51% for R2/8/17/26Q-H3-NCP or R2/8/17/26K-H3-NCP, respectively, as compared to unmodified-NCP. The higher mobility of the H3 tail within R2/8/17/26Q-H3-NCP as compared to unmodified-NCP was expected due to previous studies under non-phase-separating conditions[50] and is consistent with arginine-DNA interactions constraining the mobility of the tails. The higher mobility of the H3 tail within R2/8/17/26K-H3-NCP as compared to unmodified-NCP (albeit not as high as within R2/8/17/26Q-H3-NCP) is consistent with arginines forming stronger interactions with DNA than lysines. Similar to unmodified-NCP, there are negligible differences in R1 and hnNOE between the light and dense phases of each mutant. While the arginine-to-lysine replacement resulted in a similar overall increase in R2 values (72%) in the dense phase, arginine neutralization showed minimal differences in R2 between the two phases (11%). It seems remarkable that phase separation can occur in a sample with such minimal differences in R1, R2, and hnNOE within an IDR involved in the multivalent interactions that drive phase separation. These results with R2/8/17/26Q-H3-NCP are consistent with the

small viscosity differences between the two phases discussed above. Because there are only small differences in R1 and hnNOE between the light and dense phases of each NCP sample, the differences between these parameters upon mutation within either the light or dense phase are similar. However, there is a particularly large difference in R2 values between the dense phases of unmodified- and R2/8/17/26Q-H3-NCP (average decrease of 73%). This is consistent with a shift in the balance between intra- and inter-nucleosomal interactions within nucleosome condensates with charge-modulating modifications.

Together, these NMR data support mobility of the H3 tails on the ps-ns timescale within NCP condensates. Investigating neutralization of the four H3 tail arginines, which had the narrowest phase boundary at 25°C and the lowest viscosity, or switching the four arginines to lysines, which increased the concentration of the dense phase but decreased the viscosity, provided insight into the effect of modifications on tail dynamics. Neutralizing arginines or substituting a weaker DNA-interactor increases the mobility of the H3 tails. Differences in R2 between the two phases may report on differences in intra- vs. inter-nucleosomal interactions or the differences in viscosity (**Figure 5D**). The minimal differences between the two phases for R2/8/17/26Q-H3-NCP suggest that R2 may simply be reflecting sample viscosity. However, at this point, it cannot be determined whether: i) condensate viscosity influences tail mobility or ii) tail mobility determined by tail-DNA interactions intra- and inter-nucleosomally is involved in defining condensate viscosity. Clearly, the tail dynamics cannot solely be reflecting the condensate viscosity since the dense phase R2 values of R2/8/17/26K-H3-NCP are similar to the light phase of unmodified-NCP and the dense phase R2 values of R2/8/17/26Q-H3-NCP are well below.

## DISCUSSION

In this study, we show that nucleosome phase separation is influenced by the number, identity, and distribution of basic residues and their modifications within the H3 tail. We tested the effects of H3 tail arginine and lysine neutralization on the phase boundary and material properties of NCP condensates. Overall, neutralizations within the H3 tail decrease the phase separation propensity of the NCP by narrowing the two-phase regime of the phase boundary along with decreasing the corresponding viscosity of their condensates. Neutralizing arginines in the ‘terminal’ region of the tail have a stronger effect than in the ‘central’ region of the tail, supporting a positional dependence where residues that can reach further to bridge nucleosomes play a larger role in phase separation. In general, arginines within the H3 tail have a stronger contribution to phase separation than lysines. Shifting the H3 tail content towards lysines decreases condensate viscosity while shifting towards arginine is the one modification tested that leads to an increase in viscosity. Tail mobility within condensates correlates with viscosity, but it is currently unclear whether tail mobility determines or is determined by condensate viscosity. The strength and position of the DNA-interacting H3 tail basic residues determine phase separation propensity and properties. Thus, modifying different H3 tail basic residues has a differential direct effect on nucleosome phase separation, with implications for the direct effect of charge-modulating histone PTMs on chromatin organization via phase separation (**Figure 6**).

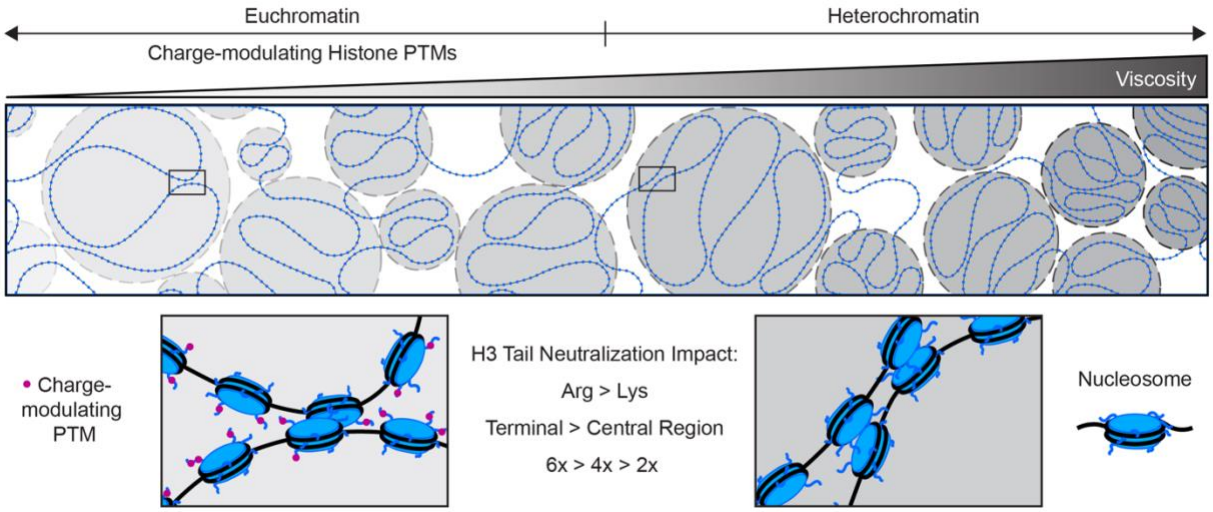


**Figure 6. Charge patterning and modifications modulate chromatin condensates.** In this model, charge-neutralizing PTMs, such as lysine acetylation and arginine citrullination, tune phase separation to lower viscosity and allow for greater access to chromatin. The differences we see in the viscosity and tail mobility of these nucleosome condensates suggest the histone language allows for different levels of accessibility by tuning the material properties of condensates. The environment and physicochemical properties of each phase-separated region of chromatin are anticipated to be determined by a combination of many nuclear factors present—chromatin, chromatin-interacting proteins, and epigenomic modifications.

Our study adds to the growing literature on the importance of the histone tails and their modifications in chromatin phase separation via both indirect and direct mechanisms. Indirect mechanisms involve chromatin-interacting proteins. Within heterochromatin, HP1 proteins, Suv39h, TRIM28, MeCP2, and PRC1 compartmentalize and compact chromatin via phase separation by binding DNA and methylated histone H3 K9 or K27 [21,51–56]. Within euchromatin, the transcriptional coactivator BRD4 and repressor PRC2 form condensates with acetylated and H3K27me3 chromatin, respectively[6,57,58]. In addition, poly(ADP-ribosyl)ated nucleosomes form condensates with proteins associated with DNA repair[59]. The histone tails are necessary for nucleosome array and NCP phase separation via direct mechanisms too, meaning, in the absence of chromatin-interacting proteins. Data to this point largely support that these phase-separation-driving interactions of the histone tails are with DNA[6,12,17]. Initial investigations of the direct effects of histone PTMs showed that non-specific hyperacetylation of histones by p300 led to the dissolution of nucleosome array condensates and neutralizing mutations of the H4 tail basic patch (specifically K16, R17, R19, and K20 to alanines) led to abrogation of phase separation in nucleosome arrays[60]. Here, our systematic perturbation of the nucleosomal H3 tails via charge-neutralizing and arginine/lysine-swapping mutations adds to our understanding of the histone language in chromatin condensates.

This systematic study perturbing H3 tail basic residues begins to address the role of charge patterning in the histone tails within the nucleosome and the effect on chromatin phase separation. Charge patterning in IDRs is important in charge-driven phase separation[61] and is relevant within the nucleus. Charge blockiness of IDRs is important in controlling which transcriptional regulators get incorporated into MED1 Mediator condensates[62]. A recent study investigated the charge patterning of the linker histone H1 C-terminal tail and its role in condensates formed with DNA[63]. The C-terminal tails of linker histones are well-mixed sequences that are lysine-rich and generally arginine-poor. In the context of the H1 C-terminal tail, higher

arginine as compared to lysine content increases phase separation propensity and decreases diffusion within the condensate (in terms of FRAP recovery). This is consistent with the higher viscosity of K4/9/14/18/23/27R-H3-NCP as compared to the unmodified-H3 sequence containing a mixture of lysine and arginine.

The H3 tails retain a high degree of mobility within the NCP condensates. Modifying arginine residues via swapping them out for a weaker DNA-interactor (i.e. lysine) or neutralization has a larger effect on ps-ns tail dynamics than the condensate environment. This highlights i) that NCP condensates minimally perturb tail mobility and ii) the role of dynamics in the histone language[50]. Biological implications of retained tail mobility include that the tails are likely not occluded by the condensate environment from interacting with regulatory proteins in, for example, a transcriptionally-active condensate. Perhaps other regulatory proteins within these nucleosome condensates are also highly mobile, but this model remains to be tested. There is precedent for the high H3 tail mobility observed in NCP condensates. Within condensates of the H1 C-terminal tail with prothymosin-α, long-range chain reconfiguration of prothymosin-α is only slowed by a factor of three while the viscosity of the condensate is 300x greater as compared to the light phase[47]. Additionally, the germ-granule protein Ddx4 forms a condensate that is ~50x more concentrated than the light phase but with similar hnNOE values[46]. This is in contrast to other systems with slowed dynamics in condensates. For example, hnRNPA2, the low-complexity domain of FUS, and an elastin-like polypeptide show larger changes in $^{15}$N-R1 and hnNOE values that are in line with a restriction in local motions[43–45].

Our results add to the emerging model of phase separation driving chromatin organization and regulation. Various nuclear factors are poised to tune condensate formation and physicochemical properties. It is anticipated that condensate viscosity influences the biological function of the compartment/subcompartment, with less viscous condensates associated with more active chromatin and vice versa[11]. If histone tail-DNA interactions dominate nucleosome phase separation, then many histone PTMs will decrease phase separation propensity and viscosity by disrupting these interactions. We propose that charge-neutralizing post-translation modifications, such as lysine acetylation and arginine citrullination, tune phase separation to lower viscosity and allow for greater access to chromatin. The differences we see in the viscosity and tail mobility of these nucleosome condensates suggest the histone language (i.e. the positions and the types of modifications) allows for different levels of accessibility by tuning the biophysical properties of condensates. Furthermore, these data suggest that PTMs may only tune chromatin phase separation in one direction, meaning to lower viscosity. We propose that, in order to tune to higher viscosity, additional condensate-promoting proteins are necessary. Variations in histone sequence (histone variants) are also poised to influence phase separation, especially by altering the composition and relative prevalence of arginine and lysine (as seen for linker histone[63]). It remains an open question whether other interactions within chromatin influence phase separation (e.g. DNA sequence and methylation, the histone core, and tail-tail interactions). Chromatin-interacting proteins are also poised to shift phase separation propensity and viscosity. These proteins and complexes can interact multivalently with chromatin to either increase or decrease phase separation propensity and are similarly expected to tune the viscosity of chromatin condensates and alter tail dynamics depending on their modes of interaction. For example, linker histone and HP1α increase the viscosity of nucleosome array or DNA condensates[6,64]. The environment and physicochemical properties of each phase-separated region of chromatin are anticipated to be determined by a combination of all nuclear factors present—chromatin, chromatin-interacting proteins, and epigenomic modifications.

## METHODS

***Expression and purification of full-length histones.*** Full-length human histone sequences were expressed and purified as previously described[12,65]. These protein sequences correspond to UniProt sequences P0C0S8, P62807, Q71DI3 (with C110A), and P62805. Briefly, each histone sequence was expressed from pET3a vectors using T7 Express lysY competent *E. coli* (New England Biolabs) or Novagen Rosetta 2(DE3) pLysS competent *E. coli* (Millipore Sigma). Mutants were generated via Q5 Site-Directed Mutagenesis Kit (New England Biolabs). The histone H3 constructs used in this study were: unmodified, R2/8Q, R17/26Q, R2/8/17/26Q, K4/9Q, K14/18/23/27Q, K4/9/18/27Q, K4/9/14/18/23/27Q, R2/8/17/26K, K4/9/14/18/23/27R, and tailless [here, referring to H3(28-135)]. Briefly, histones were extracted from inclusion bodies and purified in Urea Buffer (7 M urea, 20 mM sodium acetate pH 5.2, 100 mM NaCl, 5 mM β-ME, 1 mM EDTA) sequentially over Q-Sepharose Fast Flow resin (GE Healthcare) and SP-Sepharose Fast Flow resin (GE Healthcare) or Proteindex IEX-CM Agarose 6 Fast Flow resin (Marvelgent Biosciences). Pure histones were dialyzed into $ddH_2O$ with 1 mM β-ME and stored lyophilized at -20°C until needed for nucleosome reconstitution. ESI mass spectrometry (Finnigan LTQ, Thermo Electron Corporation, San Jose, CA) was used for histone quality assessment based on molecular weight and used to ensure no unintended modifications, such as carbamylation.

***Amplification and purification of 147 bp Widom 601 DNA.*** DNA used in both NCP reconstitution and peptide-DNA assays was obtained using a plasmid with 32 repeats of the 147-bp Widom 601 sequence (ATCGAGAATC CCGGTGCCGA GGCCGCTCAA TTGGTCGTAG ACAGCTCTAG CACCGCTTAA ACGCACGTAC GCGCTGTCCC CCGCGTTTTA ACCGCCAAGG GGATTACTCC CTAGTCTCCA GGCACGTGTC AGATATATAC ATCCGAT). Bacterial amplification and purification of 147-bp DNA was performed as previously described[12,65]. Following transformation using NEB 5-alpha Competent *E. coli* (New England Biolabs), the bacteria were grown in 2xYT media pH 7.5. The plasmid was purified using an alkaline lysis method and phenol-chloroform extractions. The 147-bp fragments were released via digestion by EcoRV-HF enzyme (New England Biolabs) and purified from the vector using PEG precipitation and HiTrap DEAE Fast Flow Columns (GE Healthcare) via FPLC (Bio-Rad). DNA purity was assessed using 5% native-PAGE gel electrophoresis. The 147-bp DNA fragments were stored following ethanol precipitation at -20°C.

***Nucleosome core particle reconstitution***. NCP reconstitutions were performed largely as previously described[12,66]. Briefly, histones H2A, H2B, H3, and H4 are individually resuspended at 2 mg/mL in Unfolding Buffer (6 M guanidine-HCl, 20 mM Tris pH 7.5, 5 mM DTT). Most histone complexes were refolded as an H2A/H2B dimer and H3/H4 tetramer, except for complexes with K4/9/14/18/23/27R-H3 and tailless-H3, which were refolded as an H2A/H2B/H3/H4 octamer. All complexes were refolded at 1 mg/mL histone via dialysis into a High Salt Buffer (2 M KCl, 20 mM Tris pH 7.5, 1 mM EDTA, 0.5 mM benzamidine, 1 mM DTT). Each histone complex was purified via FPLC using a HiLoad 16/600 Superdex 200 column (GE Healthcare), and purity was assessed using 18% SDS-PAGE gel electrophoresis. Prior to the final NCP reconstitution, purified 147-bp Widom 601 DNA was resuspended in High Salt Buffer at a final concentration of 8-11 μM. The final NCP reconstitution was performed at a molar ratio of 1:1:2.2 or 1:1:2 in terms of 147-bp Widom 601 DNA:H3/H4 tetramer:H2A/H2B dimer. For samples with K4/9/14/18/23/27R-H3 and tailless-H3, the final NCP reconstitution was performed at 1:1:0.2 molar ratio of 147-bp Widom 601 DNA:H2A/H2B/H3/H4 octamer:H2A/H2B dimer. The NCP reconstitution was performed via slow desalting with an exponential gradient followed by overnight dialysis into No Salt Buffer (20 mM Tris pH 7.5, 1 mM EDTA, 0.5 mM benzamidine, 1 mM DTT). NCPs were purified via a 10-40% sucrose gradient (BioComp Instruments). NCP purity was assessed via sucrose gradient

profile (absorbance at 260 nm) and 5% native-PAGE. Additionally, histone integrity was assessed using 18% SDS-PAGE prior to use in experiments.

***Expression and purification of H3 tail peptides***. Unmodified H3(1-44) was used as an extended histone tail peptide sequence. The following H3(1-44) mutants were also used: R2/8Q, R17/26Q, R2/8/17/26Q, K4/9Q, K14/18/23/27Q, K4/9/18/27Q, K4/9/14/18/23/27Q, R2/8/17/26K, and K4/9/14/18/23/27R. Mutant H3 tail peptides were generated using Q5 Site-Directed Mutagenesis Kit (New England Biolabs). Peptides were expressed and purified as previously described[12]. Briefly, each peptide was expressed from a pET3a vector in BL21(DE3) competent *E. coli* (New England Biolabs). Following cell lysis, the H3 tail peptides in the soluble portion were purified using Q-Sepharose Fast Flow resin (GE Healthcare) and a Source 15S column (GE Healthcare) via FPLC (Bio-Rad). Following lyophilization, peptides were purified in S30 Buffer (50mM KPi pH 7, 50mM KCl, 0.5mM EDTA) via FPLC using a HiLoad 16/600 Superdex 30 pg column (GE Healthcare). Peptides were further purified using a PROTO 300 C18 column (Higgins Analytical) via HPLC (Shimadzu). ESI mass Spectrometry (Finnigan LTQ, Thermo Electron Corporation, San Jose, CA) was used to confirm intact masses for H3 tail peptides. Peptides were lyophilized and stored at -20°C prior to experiments.

***Preparation of plates for phase separation assays.*** Prior to phase separation assays, each multiwell plate was washed with 1% Hellmanex at 30°C for 40 min, washed extensively with autoclaved $ddH_2O$, and left to air dry. Each plate was then treated with Sigmacote (Sigma-Aldrich) for 10 min, washed extensively with water, and left to air dry.

***NCP stock preparation for phase separation assays.*** NCP stocks were prepared in MOPS Buffer [20 mM MOPS pH 7 (8 mM NaOH to pH), 0.1 mM EDTA] using a 10 kDa MWCO centrifugal filtration unit (Millipore Sigma) and were stored at 4°C for a minimum of 12 hours before checking stock concentration. To determine stock concentration, a secondary NCP stock was made into MOPS Buffer. NCP concentration was determined spectrophotometrically from a 1:100 dilution of the secondary stock into 2 M KCl using a NanoDrop (Thermo Fisher). Concentration was calculated using the 147 bp Widom 601 DNA extinction coefficient at 260 nm ($\varepsilon_{260}$ = 2,312,300.9 $M^{-1}cm^{-1}$). The primary stock concentration was then back calculated.

***Turbidity assay.*** All components [NCP, H3(1-44), 601 DNA, $MgCl_2$ stock, and KCl stock] were prepared in MOPS buffer [20 mM MOPS pH 7 (with 8 mM NaOH to pH), 0.1 mM EDTA] and warmed to room temperature before conducting each assay. Final buffer conditions were 20 mM MOPS pH 7 (8 mM NaOH to pH), 0.1 mM EDTA, 150 mM KCl, and 2 mM $MgCl_2$. Note that the addition of 2 mM $MgCl_2$ is distinct from our previously-reported phase separation assays[12]. Most assays were run in µClear 96-Well Half Area Microplates (Greiner Bio-One) sealed with Optical Adhesive Film (Thermo Fisher Scientific). Absorbance measurements were recorded using a FlexStation 3 plate reader (Molecular Devices) at 600 nm ($A_{600}$) for 60 minutes at one-minute intervals. Data were recorded with a set temperature of 25°C, which had an actual experimental range of 24.9-25.6°C. The maximum $A_{600}$ value measured within the first 10 minutes of the time course was used in subsequent analyses. Data were plotted using Igor Pro (Wavemetrics) and R Statistical Software (v4.2.2; R Core Team 2022).

For assays with NCP, components were mixed in the order of MOPS buffer, KCl, $MgCl_2$, and with the final addition of concentrated NCP stock to initiate the reaction. Experiments were conducted at NCP concentrations of 0, 10, 25, 50, 100, 200, and 300 µM. Following the assay, each NCP sample was centrifuged at 18k rcf for 25 min at 25°C to separate the two phases. The NCP concentration of the upper layer (light phase, $c_L$) was determined spectrophotometrically following dilution into 2 M KCl. A total of three replicates were collected for each sample, with varied NCP concentration order between replicates. Assays were conducted at a final volume of

36.5 µL in µClear 96-Well Half Area Microplates (Greiner Bio-One) or at a final volume of 75 µL (for matched sample height) in µClear 96-Well Full Area Microplates (Greiner Bio-One).

For H3 tail and DNA, components were mixed in the order of MOPS buffer, KCl, $MgCl_2$, 147 bp 601 DNA, and with the final addition of concentrated H3(1-44) stock to initiate the reaction. Assays were performed at 50 µM H3 tail peptide with increasing DNA concentrations (0, 0.625, 1.25, 2.5, 5, 10, 12.5, 15, 25 µM) and a final volume of 20 µL in each well. Following turbidity measurements, each sample was centrifuged at 18k rcf for 25 min at 25°C, and the concentration of DNA remaining was determined spectrophotometrically following dilution into 2 M KCl.

***Brightfield microscopy.*** Images were acquired using Cytation10 Confocal Imaging Reader (Agilent) in brightfield mode with a 60x objective, collecting from -30 µm to 200 µm in 2 µm steps. Samples were prepared similar to turbidity assays. All components [NCP, H3(1-44), 601 DNA, $MgCl_2$ stock, and KCl stock] were prepared in MOPS buffer [20 mM MOPS pH 7 (with 8 mM NaOH to pH), 0.1 mM EDTA] and warmed to room temperature before conducting each assay. Final assay buffer conditions were 20 mM MOPS pH 7 (8 mM NaOH to pH), 0.1 mM EDTA, 150 mM KCl, and 2 mM $MgCl_2$. Assays used µClear 96-Well Half Area Microplates (Greiner Bio-One) sealed with Optical Adhesive Film (Thermo Fisher Scientific). Final experimental well volumes were 20 or 36.5 µL. The microscopy images were collected at room temperature with an experimental range of 27.4-28.2°C for peptide-DNA assays and 27.4-29.0°C for NCP assays. The NCP was pipetted and imaged in two ways in order to capture faster-settling condensates. The first method pipetted concentrations 0 to 300 µM in order and imaged from 0 to 300 µM. The second method pipetted concentrations 0 to 300uM in order and imaged from 300 to 0 µM. NCP microscopy replicates were conducted with n=4 for unmodified and n=3 for all mutants, which includes two biological replicates for each construct. At 300 µM NCP, phase-separated samples of R2/8/17/26Q-H3-NCP separated into two distinct layers by the time automated data collection began, with the lack of visible droplets falsely suggesting a lack of phase separation. Thus, for this mutant at 300 µM, an additional single-well experiment was collected to shorten the experiment dead time as much as possible. This single-well imaging is used in **Figure 1D**; images from both collection approaches are shown in **Supplementary Figure 1A**.

Images for figures were made using Gen5 (Agilent). Images were further analyzed using ImageJ version 2.1.0/1.54f. In an attempt to objectively define the presence of droplets in brightfield images, a pseudo-coefficient of variation (CV) was determined. The total pixel intensity values of a standard deviation z-projection and an average intensity z-projection (from 0 to 200 µm) were determined for each NCP concentration. These intensity values were baseline corrected for the buffer-only well. The reported CV was taken as the ratio of the intensities of the standard deviation projection and the average intensity projection, multiplied by 100. The CV values were averaged across replicates and plotted using R Statistical Software (v4.2.2; R Core Team 2022). A CV cutoff of 0.55 used to delineate phase separation. These values agree with a visual assessment of droplets. For H3 tail peptide and DNA, only one set of microscopy images was obtained, which were visually assessed for droplets.

***Fluorescence microscopy assay***. For fluorescence imaging of NCP samples, YOYO-1 dye (Invitrogen) was added to NCP stocks at a 1:100 molar ratio with a minimum incubation time of 16 hours prior to inducing phase separation and imaging. Samples were prepared at 200 µM NCP in a final volume of 4 µL. Final buffer conditions were 20 mM MOPS pH 7 (8 mM NaOH to pH), 0.1 mM EDTA, 150 mM KCl, and 2 mM $MgCl_2$. Samples were imaged at room temperature in µClear 384-well small volume LoBase microplates (Greiner Bio-One) sealed with optical adhesive film (Thermo Fisher Scientific). Microscopy was performed on a Nikon Eclipse Ti2-E inverted spinning disc microscope equipped with a Yokogawa confocal scanner unit (CSU-W1), 4 laser lines (405/488/568/633), a Hamamatsu ORCA-Flash4.0 V3 sCMOS Camera system with an 82% quantum efficiency chip and a water immersion dispenser. The system is run using the NIS-

Elements Advanced Research package software (version X). DIC and confocal images were collected with a z step size of 2 µm using a 60x water objective (SR Plan Apo IR). The field of view for the camera is 2048 x 2044 pixels with resolution 0.16 µm/pixel for the 60x water objective. Images were processed using Fiji and ImageJ version 2.1.0/1.54f.

***Centrifugation assays.*** A centrifugation-based assay was used to determine the phase boundary of NCPs reconstituted with unmodified and mutant H3. Phase separation was induced at 300 µM NCP and room temperature with a final volume of 30-60 µL. Final buffer conditions were 20 mM MOPS pH 7 (8 mM NaOH to pH), 0.1 mM EDTA, 150 mM KCl, and 2 mM $MgCl_2$. After allowing the sample to rest for 10 min, it was centrifuged at 18k rcf for 25 min at 25°C.

Following centrifugation, if phase separation occurred, the upper layer (light phase) was transferred to a separate tube, and both phases (now separate) were centrifuged again. Here, the concentration of the light phase was determined spectrophotometrically via NanoDrop absorbance measurement at 260 nm from three separate 1:10 dilutions in 2 M KCl. Using a Microman M25 positive displacement pipette (Gilson), 5 µL of dense phase (lower layer) was removed and transferred to 95 µL of MOPS buffer to dissipate phase separation. The concentration of this dense phase dilution was then determined by measuring absorbance at 260 nm from three separate 1:10 dilutions in 2 M KCl. Each plotted data point in Figure 1E is from one of these dilutions. If sufficient volume remained, a second dense phase measurement from this sample was obtained the same way following a repeated centrifugation step. Statistical analyses were performed using R Statistical Software (v4.2.2; R Core Team 2022). A one-way ANOVA was initially used to determine variance across modified NCPs within either the light or dense phase measurements and was determined significant with p-value of 5.37E-17 and 8.90E-59, respectively. To determine significance between modified NCPs (minimum n=4 technical replicates and two biological replicates), a post-hoc Tukey's test was used. A p-value of $<0.05$ was deemed significant for the pairwise comparisons between the NCP light phase and dense phase concentration measurements. Data were plotted using R Statistical Software (v4.2.2; R Core Team 2022).

If phase separation did not occur, the lack of two distinct layers following centrifugation was apparent. In this case, three separate 1:100 dilutions of the NCP sample were made into 2 M KCl, and the concentration was determined by measuring absorbance at 260 nm. If the concentration measured at the NCP input concentration (i.e. 300 µM), we concluded that the NCP does not phase separate under these experimental conditions. These measurements were not included in the significance analysis due to the lack of light and dense phase concentration values.

***NCP sample recovery, quality assessment, and re-use.*** Following light phase concentration measurements, NCP samples were pooled and diluted to reduce salt and dissipate NCP phase separation. Both pre-assay and post-assay NCP samples were run on 5% native-PAGE and 18% SDS-PAGE. Samples were then concentrated and exchanged into MOPS buffer using a 10 kDa MWCO centrifugal filtration unit (Millipore Sigma). Following gel confirmation and exchange, the samples were reused in replicate phase separation assays as done previously[12].

***Video particle tracking (VPT) microrheology of NCP samples.*** VPT measurements were performed on phase-separated samples of NCP variants prepared at a final NCP concentration of 200 µM in 20 mM MOPS pH 7 (8 mM NaOH to pH), 0.1 mM EDTA, 150 mM KCl, and 2 mM $MgCl_2$. Yellow-green carboxylate-modified polystyrene beads of 1 µm size were mixed during sample preparation. These beads were confirmed to partition into the dense phases of phase-separated NCP samples (**Supplementary Video 1**) and were used as probe particles for VPT measurements. The samples of volume 5 or 10 µL were sandwiched between a glass slide and coverslip treated with 5% w/v PEG in 5% ethanol. The samples were surrounded by mineral oil to prevent evaporation. The prepared sample sandwich was placed on a temperature-controlled

stage (Instec) attached to a Zeiss Primovert inverted microscope. Temperature was controlled using the thermal stage, while the actual temperature was determined using a thermocouple. The samples were allowed to fuse before imaging and rest on the microscope for 30-60 minutes before data collection. The bead motion inside the NCP dense phases was captured at 24°C in the form of videos using a 40x air objective lens and Teledyne FLIR Blackfly S USB3 CMOS camera for 1000 frames with 100 ms exposure time. The acquired videos were processed using Fiji (version 1.54f)[67]. The probe particles were tracked to get their trajectories using the Trackmate[68] software plugin in Fiji. During tracking, intensity and quality filters were used to avoid tracking aggregated particles.

The analysis routine for estimating the mean square displacement (MSDs) from particle trajectories is detailed in our previous work[69,70]. In brief, the center of the mass trajectory of the bead motion was utilized to correct the bead trajectories for any possible drift during video acquisition. The center of the mass trajectory was estimated from the velocities of the bead using

$$\boldsymbol{X_{COM}}(k) = \boldsymbol{X_0} + \sum_{j=0}^{k} \frac{1}{N_j} \sum_{i=1}^{N} \boldsymbol{v_{i,j}} \tag{1}$$

where $\boldsymbol{X_{COM}}$ is the center of mass vector calculated for $k_{\text{th}}$ frame, $j$ is the individual frame, and $N_j$ is the number of particles in the frame $j$. $\boldsymbol{X_0}$ is the center of the mass vector of the first frame. After correction, the obtained position vector of the particle $\boldsymbol{R}$ can be used to estimate the MSDs using

$$MSD(\tau) = \langle \boldsymbol{R}(t+\tau) - \boldsymbol{R}(t) \rangle_{t,N} \tag{2}$$

where $\tau$ is the lag time. We used our custom Python scripts, also deposited and can be found on GitHub (https://github.com/BanerjeeLab-repertoire/Material-properties) to compute MSD across various lag times $\tau$. The ensemble average MSD was then determined based on data from approximately 20–50 individual beads. The MSD was then fitted[69,70] using

$$MSD(\tau) = 4D\tau^{\alpha} + N \tag{3}$$

to obtain the diffusion coefficient $D$ of the beads. $\alpha$ is the diffusivity parameter which signifies the nature of bead diffusion inside the dense phases of NCP samples. For the ensemble-average MSDs for which the fitting yielded $\alpha$=1 allowed the estimation of viscosity $\eta$ using the Stokes-Einstein equation[69,70]

$$\eta = \frac{k_B T}{6\pi D R} \tag{4}$$

where $\kappa_B$ is the Boltzmann constant, $R$ is the radius of the particles, $D$ is the diffusion coefficient of beads obtained by fitting the ensemble-average MSDs to Eq. (3) and $T$ is the temperature of the sample.

The videos were recorded at 5-6 randomly chosen positions of the dense phases of NCP samples and data was collected on two technical replicates for each NCP variant. Statistical analyses were performed using R Statistical Software (v4.2.2; R Core Team 2022). To determine variance within viscosity measurements, a one-way ANOVA was initially used. Measurements obtained were determined significant with a p-value of 1.41E-33 (n=2). To determine which NCP viscosity measurements are significant to one another, a post-hoc Tukey's test was used where a p-value of <0.05 was deemed significant for the pairwise comparisons between the NCPs. Data were plotted using R.

**NMR sample preparation.** Purified NCPs reconstituted with $^{15}$N-H3 (Unmodified, R2/8/17/26Q, or R2/8/17/26K) were exchanged into MOPS buffer [20 mM MOPS pH 7 (with 8 mM NaOH to

pH), 0.1 mM EDTA] using consecutive rounds of concentration and dilution in 10k MWCO centrifugal filtration devices (Millipore Sigma). NCP stock concentration was determined spectrophotometrically via absorbance at 260 nm after diluting into 2 M KCl.

Phase separation was induced by diluting to 400 µM NCP in final solution conditions of 18 mM MOPS pH 7 (with 7.2 mM NaOH to pH), 0.09 mM EDTA, 150 mM KCl, 2 mM $MgCl_2$, and 10% $D_2O$. The sample was transferred to a 1.7 mm NMR tube (Bruker) and left to separate into two layers overnight. The top (light phase) layer was then transferred to a second 1.7 mm NMR tube. Care was taken to ensure the NMR coil volume was filled with either dense or light phase.

**NMR data collection.** Data were collected on a Bruker Avance III HD 600 MHz spectrometer with a 1.7-mm cryogenic probe at 298 K and running Topspin 3.5pl7. For chemical shift perturbation analysis, $^{1}$H-$^{15}$N HSQC spectra were collected with 16 scans, 1024 ($^{1}$H) x 300 ($^{15}$N) total points, acquisition times of 51 ms ($^{1}$H) and 75 ms ($^{15}$N), and spectra widths of ~17 ppm ($^{1}$H) and ~33 ppm ($^{15}$N). All nuclear spin relaxation experiments were collected with 1600 ($^{1}$H) x 228 ($^{15}$N) total points, acquisition times of 102 ms ($^{1}$H) and 84 ms ($^{15}$N), and spectra widths of 13 ppm ($^{1}$H) and 22 ppm ($^{15}$N). {$^{1}$H}-$^{15}$N steady-state heteronuclear nuclear Overhauser effect (hnNOE) data were collected using the Bruker pulse sequence hsqcnoef3gpsi with the reference and saturated spectra interleaved. Experiments were collected with 32 (for dense phase samples), 72 (for R2/8/17/26Q-H3 light phase sample), or 96 (for unmodified-H3 and R2/8/17/26K-H3 light phase samples) scans and an interscan delay of 5 s. The dense phase hnNOE experiments were collected at the start of the experimental queue and again 13-18 days later to check for sample aging. The data were unchanged within experimental error, and data from the initial hnNOE experiment were used in figures. Longitudinal (R1) $^{15}$N relaxation experiments were collected with total relaxation loop lengths of 0.033 s, 0.195 s, 0.390 s, 0.585 (x2), 0.813 s, 1.301 s, and 1.951 s in randomized order. Experiments were collected with 24 (for dense phase samples), 32 (for R2/8/17/26Q-H3 light phase sample), or 40 (for unmodified-H3 and R2/8/17/26K-H3 light phase samples) scans and an interscan delay of 2 s. Transverse (R2) $^{15}$N relaxation experiments were collected with an effective CPMG field of 500 Hz and total relaxation CPMG loop lengths of 0.0044 s, 0.013 s, 0.026 s, 0.044 s (x2), 0.062 s, 0.084 s, and 0.110 s. Experiments included temperature compensation blocks and were collected in randomized order, with the same number of scans as for R1, and with an interscan delay of 2.5 s. $^{1}$H-$^{15}$N HSQC spectra were collected between data series to confirm sample integrity.

**NMR data analysis.** NMRPipe and CcpNmr Analysis 2.5.2 were used within NMRbox for processing and analysis, respectively, of NMR data[71–73]. Data were plotted using Igor Pro (Wavemetrics). Amide assignments for NCPs with unmodified H3 are from BMRB entry 50806. These assignments were transferred to H3 mutants via inspection and comparison to previously-published spectra[50]. Chemical shift perturbations ($\Delta\delta$) between solution phases were calculated from the differences in amide proton ($\Delta\delta_H$) and amide nitrogen ($\Delta\delta_N$) chemical shifts using: $\Delta\delta = \sqrt{(\Delta\delta_H)^2 + (0.154\Delta\delta_N)^2}$ [74]. Spectra were processed using a cosine-squared window function for both dimensions, and each dimension was doubled in size by zero-filling twice and rounding to the nearest power of two. HnNOE values for each residue were calculated as the peak height ratio between the saturated and reference spectra, and errors were calculated via standard error propagation of the spectral noise as determined by CcpNmr Analysis 2.5.2. R1 and R2 relaxation rates were determined by fitting peak heights from the relaxation series to a single-exponential decay without offset. Errors were determined from the covariance matrix within CcpNmr Analysis 2.5.2. As discussed for previous analyses, there is the caveat resulting from the low chemical shift dispersion of IDRs that relaxation rates can be convolution by nearby peaks in dense spectral regions[50] .

**Coarse-grained molecular simulations of H3 tail with DNA fragments.** We have employed a one-bead hydrophobicity scale (HPS) model to calculate the phase diagram and viscosity of H3 tail-DNA co-condensates. The H3 tail sequence is the same as the peptide tested experimentally (ARTKQTARKSTGGKAPRKQLATKAARKSAPATGGVKKPHRYRPG). A 20-thymine (T) strand complimentary base-paired with adenine (A) was used as the DNA sequence. The two-component system comprises double-stranded DNA and H3 peptides with 40 and 44 beads, respectively. The beads in the DNA chain represent adenine-base (A) and thymine-base (T) nucleotides, and the beads in the peptide represent amino acids in H3 tail. The non-bonded interactions between residues $i$, $j$ are modeled via the Ashbaugh-Hatch potential, and salt-screened electrostatic interactions are modeled via the Debye-Huckel potential:

$$U_{ij}^{AH}(r) = \begin{cases} U^{LJ}(r) - \lambda_{ij}U^{LJ}(r_c) + \epsilon\left(1-\lambda_{ij}\right), & r \le 2^{1/6}\sigma_{ij} \\ \lambda_{ij}[U^{LJ}(r) - U^{LJ}(r_c), & 2^{1/6}\sigma_{ij} < r \le r_c \\ 0, & r > r_c \end{cases}$$

$$U_{ij}^{DH}(r) = \frac{q_i q_j e^2}{4\pi\epsilon}\frac{\exp\left(-\kappa r\right)}{r}$$

where $\epsilon$ = 0.8368 kJ/mol, $r_c$= 4 nm, and $U^{LJ}$ is the Lennard-Jones potential $U^{LJ}(r) = 4\epsilon[\left(\frac{\sigma_{ij}}{r}\right)^{12} - \left(\frac{\sigma_{ij}}{r}\right)^{6} - \sigma_{ij} = (\sigma_i + \sigma_j)/2$ and $\lambda_{ij} = (\lambda_i + \lambda_j)/2$ are arithmetic averages of monomer size and hydrophobicity value, respectively. The pair potential with $\lambda$ = 0 consists of only the repulsive term equivalent to the Weeks-Chandler-Andersen functional form. We use $\sigma$ values of amino acids from van der Waals volumes and $\lambda$ values of amino acids from the recently proposed CALVADOS 2 parameters. In the Debye-Huckel potential, $q$ is the charge number of particles and $\kappa^{-1} = \sqrt{\varepsilon k_B T/2e^2 I}$ is the Debye length. In our simulations, the ionic strength of the electrolyte $I$ = 0.17 M. The temperature-dependent dielectric constant used in our simulations has the following empirical relation: $\frac{\varepsilon(T)}{\varepsilon_0} = \frac{5321}{T} + 233.76 - 0.9297T + 1.41710 \times 10^{-3}T^2 - 8.29210 \times 10^{-7}T^3$. All coarse-grained beads are connected via bonded interactions modeled by harmonic potentials $U^{bond}(r) = \frac{k}{2}(r - r_0)^2$ where $k$ = 1000 kJ/mol/nm$^2$, $r_0$ = 0.5 nm for DNA and $r_0$ = 0.38 nm for peptide. In dsDNA, there are additional base pair interactions and stacking interactions between adjacent base-pair groups. The base pair interaction is represented by a repulsive Morse potential $U_{bp} = Dexp\left(-\alpha(r - l_0)\right)$ with $D$ = 472 kJ/mol, $\alpha$ = 2.876 nm$^{-1}$ and $l_0 = 1.243$nm. The stacking interaction is modeled using a Lennard-Jones potential, characterized by $\epsilon$ = 49.2 kJ/mol, $\sigma$ = 0.2938 nm, and a cut-off distance $r_c$ = 5.65 nm. We have applied OpenMM (v7.7) for H3 tail-DNA condensate simulations. We performed coexistence simulations in a slab geometry at different $T$ for characterizing their phase diagrams. The number of dsDNA was set at $N_{DNA}$ = 180. The number of H3 tail peptides was set around $N_{H3}$ = 520 − 720. These simulations were carried out at each $T$ for a duration of 5 × $10^7$ – 7 × $10^7$ steps, and the dense phase and dilute phase concentrations were computed based on the last 2 × $10^7$ steps of the simulation trajectory. We estimated the critical temperatures by fitting the phase diagram using the law of coexistence densities and the critical concentrations by assuming the law of rectilinear diameter holds.

We run condensate simulations in a cubic box for viscosity measurement. The number of dsDNA was set around $N_{DNA}$ = 84-180. The number of H3 tail peptides was set around $N_{H3}$ = 254 − 426 to keep the approximate charge neutrality of the co-condensates. The total number of the CG monomers was kept at about 2 × $10^4$ to eliminate the finite-size effect. The initial length of the cubic box was set at 40 nm, which is much larger than the equilibrium size. The box was then shrunk in the subsequent $NPT$ simulations. After energy minimization, we used the $NPT$ ensemble with a timestep 0.01 ps, to equilibrate all systems using additional 5 × $10^7$ steps. Finally, we fix

the box size as the average volume in $NPT$ simulations and carry out additional $NVT$ simulations for $1 \times 10^7$ steps.

## DATA AVAILABILITY

All data are available in the manuscript or the supplementary materials. Unique plasmids are available upon request.

## CODE AVAILABILITY

All analysis and calculations for VPT were done using Python scripts that are available on GitHub (https://github.com/BanerjeeLab-repertoire/Material-properties).

## REFERENCES


1. Fujishiro, S., Sasai, M. & Maeshima, K. Chromatin domains in the cell: Phase separation and condensation. *Curr. Opin. Struct. Biol.* **91**, 103006 (2025).

2. Rippe, K. Liquid–Liquid Phase Separation in Chromatin. *Csh Perspect Biol* **14**, a040683 (2022).

3. Sabari, B. R., Dall'Agnese, A. & Young, R. A. Biomolecular Condensates in the Nucleus. *Trends Biochem Sci* **45**, 961–977 (2020).

4. Shin, Y. *et al.* Liquid Nuclear Condensates Mechanically Sense and Restructure the Genome. *Cell* **175**, 1481-1491.e13 (2018).

5. Hildebrand, E. M. & Dekker, J. Mechanisms and Functions of Chromosome Compartmentalization. *Trends Biochem. Sci.* **45**, 385–396 (2020).

6. Gibson, B. A. *et al.* Organization of Chromatin by Intrinsic and Regulated Phase Separation. *Cell* **179**, 470-484.e21 (2019).

7. Narlikar, G. J. Phase-separation in chromatin organization. *J Biosciences* **45**, 5 (2020).

8. Pei, G., Lyons, H., Li, P. & Sabari, B. R. Transcription regulation by biomolecular condensates. *Nat. Rev. Mol. Cell Biol.* 1–24 (2024) doi:10.1038/s41580-024-00789-x.

9. Sabari, B. R. *et al.* Coactivator condensation at super-enhancers links phase separation and gene control. *Science* **361**, eaar3958 (2018).

10. Strom, A. R. *et al.* Phase separation drives heterochromatin domain formation. *Nature* **547**, 241–245 (2017).

11. Larson, A. G. & Narlikar, G. J. The Role of Phase Separation in Heterochromatin Formation, Function, and Regulation. *Biochemistry* **57**, 2540–2548 (2018).

12. Hammonds, E. F. *et al.* Histone H3 and H4 tails play an important role in nucleosome phase separation. *Biophys. Chem.* **283**, 106767 (2022).

13. Gibson, B. A. *et al.* In diverse conditions, intrinsic chromatin condensates have liquid-like material properties. *Proc National Acad Sci* **120**, (2023).

14. Strickfaden, H. *et al.* Condensed Chromatin Behaves like a Solid on the Mesoscale In Vitro and in Living Cells. *Cell* **183**, 1772-1784.e13 (2020).

15. Chen, Q. *et al.* Chromatin Liquid–Liquid Phase Separation (LLPS) Is Regulated by Ionic Conditions and Fiber Length. *Cells* **11**, 3145 (2022).

16. Bertin, A., Mangenot, S., Renouard, M., Durand, D. & Livolant, F. Structure and Phase Diagram of Nucleosome Core Particles Aggregated by Multivalent Cations. *Biophys J* **93**, 3652–3663 (2007).

17. Farr, S. E., Woods, E. J., Joseph, J. A., Garaizar, A. & Collepardo-Guevara, R. Nucleosome plasticity is a critical element of chromatin liquid–liquid phase separation and multivalent nucleosome interactions. *Nat Commun* **12**, 2883 (2021).

18. Millán-Zambrano, G., Burton, A., Bannister, A. J. & Schneider, R. Histone post-translational modifications — cause and consequence of genome function. *Nat Rev Genet* 1–18 (2022) doi:10.1038/s41576-022-00468-7.

19. Rothbart, S. B. & Strahl, B. D. Interpreting the language of histone and DNA modifications. *Biochimica Et Biophysica Acta Bba - Gene Regul Mech* **1839**, 627–643 (2014).

20. Tolsma, T. O. & Hansen, J. C. Post-translational modifications and chromatin dynamics. *Essays Biochem* **63**, 89–96 (2019).

21. Wang, L. *et al.* Histone Modifications Regulate Chromatin Compartmentalization by Contributing to a Phase Separation Mechanism. *Molecular cell* **76**, 646-659.e6 (2019).

22. Nitsch, S., Shahidian, L. Z. & Schneider, R. Histone acylations and chromatin dynamics: concepts, challenges, and links to metabolism. *Embo Rep* **22**, e52774 (2021).

23. Fuhrmann, J., Clancy, K. W. & Thompson, P. R. Chemical Biology of Protein Arginine Modifications in Epigenetic Regulation. *Chem Rev* **115**, 5413–5461 (2015).

24. Mascotti, D. P. & Lohman, T. M. Thermodynamics of Oligoarginines Binding to RNA and DNA †. *Biochemistry-us* **36**, 7272–7279 (1997).

25. Wintjens, R., Liévin, J., Rooman, M. & Buisine, E. Contribution of cation-π interactions to the stability of protein-DNA complexes11Edited by J. Thornton. *J Mol Biol* **302**, 393–408 (2000).

26. Rohs, R. *et al.* The role of DNA shape in protein-DNA recognition. *Nature* **461**, 1248–1253 (2009).

27. DeRouchey, J., Hoover, B. & Rau, D. C. A Comparison of DNA Compaction by Arginine and Lysine Peptides: A Physical Basis for Arginine Rich Protamines. *Biochemistry-us* **52**, 3000–3009 (2013).

28. Leng, M. & Felsenfeld, G. The preferential interactions of polylysine and polyarginine with specific base sequences in DNA. *Proc. Natl. Acad. Sci.* **56**, 1325–1332 (1966).

29. Lenton, S. *et al.* Impact of Arginine–Phosphate Interactions on the Reentrant Condensation of Disordered Proteins. *Biomacromolecules* (2021) doi:10.1021/acs.biomac.0c01765.

30. Alshareedah, I. *et al.* Interplay between Short-Range Attraction and Long-Range Repulsion Controls Reentrant Liquid Condensation of Ribonucleoprotein–RNA Complexes. *J Am Chem Soc* **141**, 14593–14602 (2019).

31. Boeynaems, S. *et al.* Spontaneous driving forces give rise to protein−RNA condensates with coexisting phases and complex material properties. *Proc National Acad Sci* **116**, 201821038 (2019).

32. Fisher, R. S. & Elbaum-Garfinkle, S. Tunable multiphase dynamics of arginine and lysine liquid condensates. *Nat Commun* **11**, 4628 (2020).

33. Li, Z. & Kono, H. Distinct Roles of Histone H3 and H2A Tails in Nucleosome Stability. *Scientific reports* **6**, srep31437 (2016).

34. Peng, Y., Li, S., Onufriev, A., Landsman, D. & Panchenko, A. R. Binding of regulatory proteins to nucleosomes is modulated by dynamic histone tails. *Nat Commun* **12**, 5280 (2021).

35. Morrison, E. A., Bowerman, S., Sylvers, K. L., Wereszczynski, J. & Musselman, C. A. The conformation of the histone H3 tail inhibits association of the BPTF PHD finger with the nucleosome. *Elife* **7**, e31481 (2018).

36. Pepenella, S., Murphy, K. J. & Hayes, J. J. Intra- and inter-nucleosome interactions of the core histone tail domains in higher-order chromatin structure. *Chromosoma* **123**, 3–13 (2013).

37. Morrison, E. A., Baweja, L., Poirier, M. G., Wereszczynski, J. & Musselman, C. A. Nucleosome composition regulates the histone H3 tail conformational ensemble and accessibility. *Nucleic Acids Res* **49**, gkab246- (2021).

38. Banerjee, P. R., Milin, A. N., Moosa, M. M., Onuchic, P. L. & Deniz, A. A. Reentrant Phase Transition Drives Dynamic Substructure Formation in Ribonucleoprotein Droplets. *Angewandte Chemie Int Ed* **56**, 11354–11359 (2017).

39. Teif, V. B. & Bohinc, K. Condensed DNA: Condensing the concepts. *Prog Biophysics Mol Biology* **105**, 208–222 (2011).

40. Nguyen, T. T. & Shklovskii, B. I. Complexation of DNA with positive spheres: Phase diagram of charge inversion and reentrant condensation. *J Chem Phys* **115**, 7298–7308 (2001).

41. Alshareedah, I. *et al.* Sequence-specific interactions determine viscoelasticity and ageing dynamics of protein condensates. *Nat. Phys.* **20**, 1482–1491 (2024).

42. Sanfeliu-Cerdán, N. & Krieg, M. The mechanobiology of biomolecular condensates. *Biophys. Rev.* **6**, 011310 (2025).

43. Ryan, V. H. *et al.* Mechanistic View of hnRNPA2 Low-Complexity Domain Structure, Interactions, and Phase Separation Altered by Mutation and Arginine Methylation. *Molecular cell* **69**, 465-479.e7 (2018).

44. Burke, K. A., Janke, A. M., Rhine, C. L. & Fawzi, N. L. Residue-by-Residue View of In Vitro FUS Granules that Bind the C-Terminal Domain of RNA Polymerase II. *Molecular cell* **60**, 231–241 (2015).

45. Reichheld, S. E., Muiznieks, L. D., Keeley, F. W. & Sharpe, S. Direct observation of structure and dynamics during phase separation of an elastomeric protein. *Proc. Natl. Acad. Sci.* **114**, E4408–E4415 (2017).

46. Brady, J. P. *et al.* Structural and hydrodynamic properties of an intrinsically disordered region of a germ cell-specific protein on phase separation. *Proc. Natl. Acad. Sci.* **114**, E8194–E8203 (2017).

47. Galvanetto, N. *et al.* Extreme dynamics in a biomolecular condensate. *Nature* **619**, 876–883 (2023).

48. Tsunaka, Y., Furukawa, A. & Nishimura, Y. Histone tail network and modulation in a nucleosome. *Curr Opin Struc Biol* **75**, 102436 (2022).

49. Ghoneim, M., Fuchs, H. A. & Musselman, C. A. Histone Tail Conformations: A Fuzzy Affair with DNA. *Trends Biochem Sci* (2021) doi:10.1016/j.tibs.2020.12.012.

50. Jennings, C. E., Zoss, C. J. & Morrison, E. A. Arginine anchor points govern H3 tail dynamics. *Frontiers Mol Biosci* **10**, 1150400 (2023).

51. Strom, A. R. *et al.* Phase separation drives heterochromatin domain formation. *Nature* **547**, 241–245 (2017).

52. Larson, A. G. *et al.* Liquid droplet formation by HP1α suggests a role for phase separation in heterochromatin. *Nature* **547**, 236–240 (2017).

53. Zhao, S. *et al.* Plant HP1 protein ADCP1 links multivalent H3K9 methylation readout to heterochromatin formation. *Cell Res* **29**, 54–66 (2019).

54. Wang, L. *et al.* Rett syndrome-causing mutations compromise MeCP2-mediated liquid–liquid phase separation of chromatin. *Cell Res* **30**, 393–407 (2020).

55. Tatavosian, R. *et al.* Nuclear condensates of the Polycomb protein chromobox 2 (CBX2) assemble through phase separation. *J Biol Chem* **294**, 1451–1463 (2019).

56. Plys, A. J. *et al.* Phase separation of Polycomb-repressive complex 1 is governed by a charged disordered region of CBX2. *Gene Dev* **33**, 799–813 (2019).

57. Han, X. *et al.* Roles of the BRD4 short isoform in phase separation and active gene transcription. *Nat. Struct. Mol. Biol.* **27**, 333–341 (2020).

58. Lu, G. & Li, P. PHF1 compartmentalizes PRC2 via phase separation. *Biochem. J.* **480**, 1833–1844 (2023).

59. Nosella, M. L. *et al.* Poly(ADP-ribosyl)ation enhances nucleosome dynamics and organizes DNA damage repair components within biomolecular condensates. *Mol. Cell* **84**, 429-446.e17 (2024).

60. Gibson, B. A. *et al.* Organization of Chromatin by Intrinsic and Regulated Phase Separation. *Cell* 1–37 (2019) doi:10.1016/j.cell.2019.08.037.

61. Chang, L.-W. *et al.* Sequence and entropy-based control of complex coacervates. *Nat. Commun.* **8**, 1273 (2017).

62. Lyons, H. *et al.* Functional partitioning of transcriptional regulators by patterned charge blocks. *Cell* **186**, 327-345.e28 (2023).

63. Watson, M. *et al.* A DNA condensation code for linker histones. *Proc. Natl. Acad. Sci.* **121**, (2024).

64. Keenen, M. M. *et al.* HP1 proteins compact DNA into mechanically and positionally stable phase separated domains. *Elife* **10**, e64563 (2021).

65. Paintsil, E. A. & Morrison, E. A. DNA-Protein Interactions, Methods and Protocols. *Methods Mol Biology* **2599**, 163–175 (2022).

66. Hammonds, E. F. & Morrison, E. A. DNA-Protein Interactions, Methods and Protocols. *Methods Mol. Biol.* **2599**, 177–190 (2022).

67. Schindelin, J. *et al.* Fiji: an open-source platform for biological-image analysis. *Nat Methods* **9**, 676–682 (2012).

68. Tinevez, J.-Y. *et al.* TrackMate: An open and extensible platform for single-particle tracking. *Methods* **115**, 80–90 (2017).

69. Alshareedah, I., Moosa, M. M., Pham, M., Potoyan, D. A. & Banerjee, P. R. Programmable viscoelasticity in protein-RNA condensates with disordered sticker-spacer polypeptides. *Nat. Commun.* **12**, 6620 (2021).

70. Alshareedah, I. *et al.* Determinants of viscoelasticity and flow activation energy in biomolecular condensates. *Sci. Adv.* **10**, eadi6539 (2024).

71. Maciejewski, M. W. *et al.* NMRbox: A Resource for Biomolecular NMR Computation. *Biophys J* **112**, 1529–1534 (2017).

72. Delaglio, F. *et al.* NMRPipe: a multidimensional spectral processing system based on UNIX pipes. *Journal of biomolecular NMR* **6**, 277–293 (1995).

73. Vranken, W. F. *et al.* The CCPN data model for NMR spectroscopy: development of a software pipeline. *Proteins* **59**, 687–696 (2005).

74. Tugarinov, V. & Kay, L. E. Quantitative NMR studies of high molecular weight proteins: application to domain orientation and ligand binding in the 723 residue enzyme malate synthase G. *Journal of molecular biology* **327**, 1121–1133 (2003).

## ACKNOWLEDGMENTS

Research reported in this publication was supported by the National Institute of General Medical Sciences of the US National Institutes of Health (NIH) under Award Number R35 GM142594 (to E.A.M) and by an NIH Shared Instrumentation Grant to the MCW NMR Facility under Award Number S10OD020000. This study made use of NMRbox: National Center for Biomolecular NMR Data Processing and Analysis, a Biomedical Technology Research Resource (BTRR), which is supported by NIH grant P41GM111135 (NIGMS). Research contributions from the Banerjee laboratory were supported by the US National Institutes of Health (NIH) through a grant award R35 GM138186 (to P.R.B). Research contributions from the Potoyan laboratory were supported by the National Institutes of Health with grant R35 GM138243 (to D.A.P.). The funders had no role in study design, data collection and analysis, decision to publish, or preparation of the manuscript. The content is solely the responsibility of the authors and does not necessarily represent the official views of the National Institutes of Health. Thanks to Drs. Catherine Musselman, Karolin Luger, and Michael Poirier for gifts of histone plasmids.

## AUTHOR CONTRIBUTIONS

EM conceived of the initial project. EH, EM, DP, and PB designed the studies. EM, DP, and PB acquired funding and supervised the research. EH and SMZ prepared samples. EH, AS, KS, SY, RG, and EM performed the research and analyzed the data. EH, AS, KS, and EM visualized the data. EH and EM wrote the manuscript with contributions from AS, KS, DP, and PB.

## COMPETING INTERESTS

P.R.B. is a member of the Biophysics Reviews (AIP Publishing) editorial board. This affiliation did not influence the work reported here. All other authors declare that the research was conducted in the absence of any commercial or financial relationships that could be construed as a potential conflict of interest.

## MATERIALS & CORRESPONDENCE

Correspondence on microrheology measurements should be addressed to Priya Banerjee at prbanerj@buffalo.edu. Correspondence on simulations should be addressed to David Potoyan at potoyan@iastate.edu. Other correspondence and material requests should be addressed to Emma Morrison at emorrison@mcw.edu.